Defense Threat Reduction Agency
8725 John J. Kingman Road, MS-6201
Fort Belvoir, VA 22060-6201

DTRA-TR-14-74

TECHNICAL REPORT

On the Radiation Effect in Nanostructures Related to Nanomagnetics and Spintronics

Approved for public release; distribution is unlimited.

March 2015

HDTRA1-11-1-0024

Jiwei Lu

Prepared by:
University of Virginia
P.O. Box 400745
395 McCormick Road
Charlottesville, VA 22904

DESTRUCTION NOTICE:

Destroy this report when it is no longer needed.
Do not return to sender.

PLEASE NOTIFY THE DEFENSE THREAT REDUCTION AGENCY, ATTN: DTRIAC/ J9STT, 8725 JOHN J. KINGMAN ROAD, MS-6201, FT BELVOIR, VA 22060-6201, IF YOUR ADDRESS IS INCORRECT, IF YOU WISH THAT IT BE DELETED FROM THE DISTRIBUTION LIST, OR IF THE ADDRESSEE IS NO LONGER EMPLOYED BY YOUR ORGANIZATION.

REPORT DOCUMENTATION PAGE

Form Approved
OMB No. 0704-0188

Public reporting burden for this collection of information is estimated to average 1 hour per response, including the time for reviewing instructions, searching existing data sources, gathering and maintaining the data needed, and completing and reviewing this collection of information. Send comments regarding this burden estimate or any other aspect of this collection of information, including suggestions for reducing this burden to Department of Defense, Washington Headquarters Services, Directorate for Information Operations and Reports (0704-0188), 1215 Jefferson Davis Highway, Suite 1204, Arlington, VA 22202-4302. Respondents should be aware that notwithstanding any other provision of law, no person shall be subject to any penalty for failing to comply with a collection of information if it does not display a currently valid OMB control number. **PLEASE DO NOT RETURN YOUR FORM TO THE ABOVE ADDRESS.**

1. REPORT DATE *(DD-MM-YYYY)*
00-03-2015

2. REPORT TYPE
Technical

3. DATES COVERED *(From - To)*
June 24, 2011 - June 28, 2014

4. TITLE AND SUBTITLE
On the Radiation Effect in Nanostructures Related to Nanomagnetics and Spintronics

5a. CONTRACT NUMBER
HDTRA1-11-1-0024

5b. GRANT NUMBER

5c. PROGRAM ELEMENT NUMBER

6. AUTHOR(S)
Jiwei Lu

5d. PROJECT NUMBER

5e. TASK NUMBER

5f. WORK UNIT NUMBER

7. PERFORMING ORGANIZATION NAME(S) AND ADDRESS(ES)
University of Virginia
P.O. Box 400745
395 McCormick Road
Charlottesville, VA 22904

8. PERFORMING ORGANIZATION REPORT NUMBER

9. SPONSORING / MONITORING AGENCY NAME(S) AND ADDRESS(ES)
Defense Threat Reduction Agency
8725 John J. Kingman Road STOP 6201
Fort Belvoir, VA 22060
PM/Allison Lyalikov

10. SPONSOR/MONITOR'S ACRONYM(S)
DTRA

11. SPONSOR/MONITOR'S REPORT NUMBER(S)
DTRA-TR-14-74

12. DISTRIBUTION / AVAILABILITY STATEMENT
Approved for public release; distribution is unlimited.

13. SUPPLEMENTARY NOTES

14. ABSTRACT

In the frame of this project, we not only have advanced the understanding on radiation effects on spin transport related properties in novel magnetic materials, but also evaluated the next generation STT-RAM technology for "Rad Hard" that is essential to DTRA's mission. The overall goal is to investigate effects of displacement and ionization damages on the magnetic and structural properties of magnetic thin films and nanostructures, and to understand what factors control the radiation hardness of high-performance magnetic thin films and multilayers in nanoscale spin-based devices. To achieve these goals, a holistic approach has been taken to characterize the properties and microstructure of the thin films and spintronic devices and perform the modeling and simulation to help understanding the underlying physics of experimental phenomena by an interdisciplinary team with expertise on Materials Science, Device Physics, and Radiation Physics. We have systematically investigated the displacement and ionization damages to the perpendicular magnetic tunnel junctions (p-MTJ), and also studied the effect of irradiations on novel magnetic materials.

15. SUBJECT TERMS
Radiation Nanostructures Rad Hard Magnetic Spintronics

16. SECURITY CLASSIFICATION OF:			**17. LIMITATION OF ABSTRACT**	**18. NUMBER OF PAGES**	**19a. NAME OF RESPONSIBLE PERSON**
a. REPORT	**b. ABSTRACT**	**c. THIS PAGE**	SAR	27	Allison Lyalikov
Unclassified	Unclassified	Unclassified			**19b. TELEPHONE NUMBER** *(include area code)* 703-767-4663

Standard Form 298 (Rev. 8-98)
Prescribed by ANSI Std. Z39.18

CONVERSION TABLE

Conversion Factors for U.S. Customary to metric (SI) units of measurement.

MULTIPLY → BY → TO GET

TO GET ← BY ← DIVIDE

angstrom	1.000 000 x E -10	meters (m)
atmosphere (normal)	1.013 25 x E +2	kilo pascal (kPa)
bar	1.000 000 x E +2	kilo pascal (kPa)
barn	1.000 000 x E -28	meter^2 (m^2)
British thermal unit (thermochemical)	1.054 350 x E +3	joule (J)
calorie (thermochemical)	4.184 000	joule (J)
cal (thermochemical/cm^2)	4.184 000 x E -2	mega joule/m^2 (MJ/m^2)
curie	3.700 000 x E +1	*giga bacquerel (GBq)
degree (angle)	1.745 329 x E -2	radian (rad)
degree Fahrenheit	$t_k = (t^of + 459.67)/1.8$	degree kelvin (K)
electron volt	1.602 19 x E -19	joule (J)
erg	1.000 000 x E -7	joule (J)
erg/second	1.000 000 x E -7	watt (W)
foot	3.048 000 x E -1	meter (m)
foot-pound-force	1.355 818	joule (J)
gallon (U.S. liquid)	3.785 412 x E -3	meter^3 (m^3)
inch	2.540 000 x E -2	meter (m)
jerk	1.000 000 x E +9	joule (J)
joule/kilogram (J/kg) radiation dose absorbed	1.000 000	Gray (Gy)
kilotons	4.183	terajoules
kip (1000 lbf)	4.448 222 x E +3	newton (N)
kip/inch^2 (ksi)	6.894 757 x E +3	kilo pascal (kPa)
ktap	1.000 000 x E +2	newton-second/m^2 (N-s/m^2)
micron	1.000 000 x E -6	meter (m)
mil	2.540 000 x E -5	meter (m)
mile (international)	1.609 344 x E +3	meter (m)
ounce	2.834 952 x E -2	kilogram (kg)
pound-force (lbs avoirdupois)	4.448 222	newton (N)
pound-force inch	1.129 848 x E -1	newton-meter (N-m)
pound-force/inch	1.751 268 x E +2	newton/meter (N/m)
pound-force/foot^2	4.788 026 x E -2	kilo pascal (kPa)
pound-force/inch^2 (psi)	6.894 757	kilo pascal (kPa)
pound-mass (lbm avoirdupois)	4.535 924 x E -1	kilogram (kg)
pound-mass-foot^2 (moment of inertia)	4.214 011 x E -2	kilogram-meter^2 (kg-m^2)
pound-mass/foot^3	1.601 846 x E +1	kilogram-meter^3 (kg/m^3)
rad (radiation dose absorbed)	1.000 000 x E -2	**Gray (Gy)
roentgen	2.579 760 x E -4	coulomb/kilogram (C/kg)
shake	1.000 000 x E -8	second (s)
slug	1.459 390 x E +1	kilogram (kg)
torr (mm Hg, 0^0 C)	1.333 22 x E -1	kilo pascal (kPa)

*The bacquerel (Bq) is the SI unit of radioactivity; 1 Bq = 1 event/s.

**The Gray (GY) is the SI unit of absorbed radiation.

Final Technical Report

Project Title:

On the radiation effect in nanostructures related to nanomagnetics and spintronics

Grant/Award #: HDTRA1-11-1-0024
PI Name: Jiwei Lu
Organization/Institution: University of Virginia

I. Summary

In the frame of this project, we not only have advanced the understanding on **radiation effects** on spin transport related properties in ***novel magnetic materials***, but also evaluated the next generation STT-RAM technology for ***"Rad Hard"*** that is essential to DTRA's mission. The overall goal is to investigate effects of displacement and ionization damages on the magnetic and structural properties of magnetic thin films and nanostructures, and to understand what factors control the radiation hardness of high-performance magnetic thin films and multilayers in nanoscale spin-based devices. To achieve these goals, a holistic approach has been taken to characterize the properties and microstructure of the thin films and spintronic devices and perform the modeling and simulation to help understanding the underlying physics of experimental phenomena by an interdisciplinary team with expertise on **Materials Science**, **Device Physics**, and **Radiation Physics**. We have systematically investigated the displacement and ionization damages to the perpendicular magnetic tunnel junctions (p-MTJ), and also studied the effect of irradiations on novel magnetic materials. Through this project, we have also explored the synthesis and magnetic properties of RE-TM alloys that are promising for ultra-fast lighted assisted magnetization switching, and discovered interesting and strange magneto-transport properties needed further investigation.

The project has supported 4 PIs, two graduate student at the University of Virginia, and 4 technical staff members (partial support) at Grandis. There are 6 publications and manuscripts. There are 8 conference presentations, 3 invited talks that are the results of direct support of this project.

II. Participant Individuals:

Senior personnel: Jiwei Lu (PI), Joe Poon (co-PI), Bradley Weaver (co-PI), Eugene Chen (co-PI)

Graduate students supported by this project: Nattawut Anuniwat (Ph.D., expected in Summer 2014), Xiaopu Li (Ph.D., expected 2016),

Graduate and undergraduate students involved with this project: Yishen Cui (Ph.D., 2013), Manli

Ding (Ph.D., 2012), Kaitlyn Bock (B.S., Spring 2012), Marc Costantine (M.S.).
Collaborators: Stu Wolf, Patrick Hopkins (University of Virginia), Tim Mewes (University of Alabama), Harold Hughes, Patrick McMarr (Naval Research Laboratory).

III. Major activities.

This project has three technical areas working very closely together to meet the overall goals of this effort.

Magnetic nanostructures and materials: We investigated two types of nanostructures for the irradiation. Grandis fabricated the pMTJ films and pMTJ device wafers for the irradiation. The second structure is a nanowire device made from PMA magnetic thin films which was fabricated and characterized at UVA. We have synthesized thin films manganese-aluminum (Mn-Al), and rare earth-iron-cobalt (RE-Fe-Co) with very perpendicular magnetic anisotropy, which is of interest for high performance low power STT-RAM. These material systems offer a variety of magnetic properties and crystalline/amorphous structures for a systematic study. For amorphous RE-Fe-Co systems, the strong perpendicular magnetic anisotropy (PMA) is investigated by Monte Carlo modeling, and the energetic proton beam is used as a probe to examine the origin of PMA, which will be described in details below.

Displacement Damage: For magnetic materials and nanostructures, the main radiation effect is expected to arise from displacement damage. The effects on magnetic devices are largely unknown, and this project provides an insight to the effect of irradiation on the magnetic and magneto-transport properties of thin films and nanostructures. We performed 2 MeV proton irradiations on various structured magnetic materials including GdFeCo, TbFeCo and L10 MnAl using particle fluences between $1x10^{14}$ and $5x10^{15}$ H^+/cm^2. Samples were irradiated with 2 MeV protons at the tandem Van de Graaf accelerator at Auburn University. There was not intentional heating during the irradiation process. The energy was selected so that particles would traverse the entire sample without significant loss of energy, thereby creating a uniform profile of defects. The defects created are mainly vacancies, interstitials and Frenkel pairs. An initial fluence Φ of $1x10^{14}$ 2 MeV H^+/cm^2 was used. Following the initial irradiation the samples were re-characterized then irradiated in increments to a total fluence up to 2×10^{15} H^+/cm^2. SRIM (Stopping and Range of Ions in Matter) simulation is used to simulate the depth profile and energy loss of protons, and the defect creation in both thin films and nanostructures such as perpendicular magnetic tunnel junctions (PMTJ).

Characterization and evaluation: We employ a suite of tools to characterize magnetic properties, and spin dependent transport properties of nanostructures, particularly the properties related to the spin torque transfer. The microstructures of thin films and nanostructures are also characterized, and the effect of the irradiation is correlated to the evolution of structures and properties through the simulation results.

IV. Specific objectives.

Task 1 Development of magnetic nanostructures and thin films.

- Synthesize and investigate novel magnetic materials with strong perpendicular magnetic anisotropy.
- Fabricate nanowires and demonstrate the current driven magnetic domain wall motion with PMA materials.
- Deposit the same key individual layers (starting immediately) or the whole Perpendicular MTJ (PMTJ) structures used for STT-RAM.
- Fabricate Grandis deposited PMTJ films to devices to evaluate the STT switching performances, as well as TMR ratio and resistance values of the PMTJ devices.

Task 2 Irradiation of magnetic nanostructures and thin films.

- Provide irradiations for controlled defect formation
- Support the overall project by performing simulations of radiation damage
- Accumulate radiation effects expertise in this new area of research

Task 3 Characterizations of irradiated magnetic thin films and nanostructures.

- Quantify the defect density, the intermixing and the other changes in the chemical ordering after the irradiation.
- Establish the understanding of the nanosize effect and effect due to extrinsic defects on magnetic properties, and multilayer films for effect due to interlayer mixing and formation of interfacial layers
- Determine the origin of magnetic anisotropy in RE-TM systems.
- Compare the spin dependent transport properties, the tunnel barrier resistances of MTJs and DWM devices post-irradiation to the results measured in Task 1.
- Develop the scientific principles for improving the radiation hardness of magnetic nanostructures.

V. Scientific communications

(i) Publication and manuscripts

1. P. E. Hopkins, M. Ding, S. J. Poon, Contributions of electron and phonon transport to the thermal conductivity of GdFeCo and TbFeCo amorphous rare-earth transition-metal alloys, Journal of Applied Physics 111, 103533 (2012).
2. N. Anuniwat, Y. Cui, S. A. Wolf, J. W. Lu and B. D. Weaver, Recovery of the chemical ordering in $L1_0$ MnAl epitaxial thin films irradiated by 2 MeV protons, Applied Physics Letter, 102, 102406 (2013)
3. N. Anuniwat, M. Ding, S. J. Poon, S. A. Wolf and J. W. Lu, Strain-induced enhancement of coercivity in amorphous TbFeCo, Journal of Applied Physics, 113, 043905 (2013)
4. Magneto-transport properties of GdFeCo metglass near compensation point
5. Effect of proton irradiation on the magnetic and magneto-transport properties of perpendicular magnetic tunnel junctions, to be submitted.
6. Effect of proton irradiation on the magnetic and magneto-transport properties of TbFeCo

metglass, to be submitted.

(ii) Invited talks

1. Radiation Effect on the Magnetism and the Spin- Dependent Transport in Ferromagnetic L10 MnAl, J Lu, et al. GOMACTech-12, Las Vegas, NV, 2012
2. "Novel Materials for Spin Torque Transfer- Random Access memory", J. Lu, Data Storage Institute, Singapore, July 2013. (Invited seminar talk).
3. "Novel magnetic films to support DTRA mission", S. J. Poon, UVA NanoStar Spring Symposium, Charlottesville, VA, June 2013 (Invited oral talk).

(iii) Conference presentations

1. "Anomalous Magneto Transport in amorphous TbFeCo thin films", N Anuniwat, M Costantine, J Lu, M Ding, J Poon, APS march meeting, Boston, MA, 2012
2. "Magnetic Characterization of heavily proton-irradiated MnAl Hall bars", M Costantine, et al., APS march meeting, Boston, MA, 2012
3. "Effect of proton irradiation on the magnetic and magneto-transport properties of TbFeCo metglass", N. Anuniwat et al. American Physical Society March Meeting, Baltimore, MD March 2013 (Oral presentation)
4. "Anomalous Magneto Transport in Amorphous TbFeCo Film with Perpendicular Magnetic Anisotropy, N. Anuniwat, et al., AVS 59th International Symposium and Exhibition, Tampa, FL, October 2012 (Oral presentation)
5. "Radiation Effects on the Magnetism and the Magneto-transport in Novel Magnetic Materials", N. Anuniwat, et al., DTRA annual review, Springfield, VA, July 2012 (poster).
6. "Effect of displacement damages on physical properties of amorphous TbFeCo thin films", J. Lu et al. American Physical Society March Meeting, Denver, Co March 2014 (Oral presentation)
7. "Magnetoresistive anomaly in amorphous GdFeCo thin films", N. Anuniwat et al. American Physical Society March Meeting, Denver, Co March 2014 (Oral presentation)
8. "Monte Carlo Simulation of GdFeCo Amorphous Films with Perpendicular Magnetic Anisotropy", X. Li et al., American Physical Society March Meeting, Denver, Co March 2014 (Oral presentation)

VI. Significant results

(i) Recovery of chemical ordering in highly ordered L_10 MnAl via proton irradiation

Among a variety of PMA materials like FePt and CoPt, magnetic MnAl with a high bulk magnetization around 490 emu/cc and a uniaxial crystalline anisotropy has been considered as the promising PMA candidate without any noble metals, i.e. platinum and palladium. Nonetheless, the main challenge remains in synthesizing magnetic MnAl thin films because this ferromagnetic tetragonal $L1_0$ structure (τ phase) in MnAl is a metastable phase that only forms in a very small window of chemical composition, and the growth of thin films could be even more sensitive to growth parameters such as deposition techniques and seeding substrates.

Synthesis: MnAl films were synthesized using a Biased Target Ion Beam Deposition system (BTIBD). BTIBD uses a low energy ion source that combines an end-Hall ion source and a hollow cathode electron source, which produces a high density of inert gas ions with low energies (5 - 50 eV). By applying a negative potential bias (-100 to -1200V), the ions are accelerated towards the metal target with energies high enough to induce sputtering. The base pressure of BTIBD chamber was below 8 x 10^{-8} torr. Cubic MgO (001) substrates were selected to provide a seeding effect due to the small lattice mismatch between MgO and τ phase MnAl. The details of the synthesis can be found elsewhere. A tantalum layer was deposited as the capping layer to prevent MnAl films from oxidation. The samples were further treated with Rapid Thermal Annealing (As–One100) in vacuum (~1.5 x 10^{-5} torr), at 400˚C for 12 seconds.
Characterization: The sample composition was determined by Rutherford backscattering spectroscopy (RBS) with the Mn atomic percentage of 50.6 at. %, which fell in the window of τ phase MnAl (50%-60%) in the Mn-Al phase diagram. The film thicknesses and structural properties were characterized with a high resolution X-Ray diffractometer with Cu Kα radiation (Smart-lab®, Rigaku Inc.). The in-plane and out-of-plane hysteresis loops were measured with the VSM option using the Quantum Design PPMS-6000. In particular, the out-of-plane coercivity field was characterized using a polar Magneto-Optic Kerr Effect looper (MOKE). To measure the spin dependent transport, Hall devices were fabricated by photolithography and the width of the Hall bar was ~2 μm.
Irradiation: Following the initial characterization samples were irradiated with 2 MeV protons at the tandem Van de Graaf accelerator at Auburn University. The energy was selected so that particles would traverse the entire sample without significant loss of energy, thereby creating a uniform profile of defects. The defects created are mainly vacancies, interstitials and Frenkel pairs. The initial fluence Φ of 10^{14} 2 MeV H^+/cm^2 was chosen to be quite large because the MnAl films under study contain many pre-existing defects, and a baseline for the radiation response is necessary before the materials are fabricated into devices. For comparison, the initial fluence was equivalent to a total dose of about 100 Mrad(Si). Following the initial irradiation the samples were re-characterized then exposed to additional irradiations for a total fluence of 2×10^{15} H^+/cm^2. The information on the irradiation experiments was listed in Table 1.
Key results: XRD spectra taken from the same sample through the irradiation process was used to calculate the chemical ordering of MnAl thin films. The chemical ordering was extracted and tabulated in Table 1. The ***S*** value of the pre-irradiation sample was ~0.97, indicating a very high chemical ordering for MnAl films as the result of post-deposition annealing. ***S*** was reduced to ~0.8 after the irradiation with a fluence of 1×10^{14} 2 MeV H^+/cm^2, and further down to ~ 0.72 when the fluence increased to 1×10^{15} $/cm^2$. After the 3rd irradiation, the change in the chemical ordering was reversed and ***S*** became ~ 0.81. Table 1 also lists the peak position and the FWHM (full width hall maximum) of (001) and (002) from MnAl films respectively. The positions of these two peaks did not show any significant changes during the irradiation process. On the other hand, the FWHM increased and reached a maximum after the second irradiation with the

total fluence of 1×10^{15} cm^{-2}. At the final fluence of 2×10^{15} cm^{-2}, the FWHM was slightly reduced for both (001) and (002) peaks.

Table 1. Chemical ordering (*S*) and peak parameters of (001) and (002) extracted from XRD spectra

Total fluence (H^+/cm^2)	*S*	(001)		(002)	
		2θ	FWHM	2θ	FWHM
0	0.97	29.932±0.004°	0.715±0.004°	62.241±0.010°	1.317±0.021°
1×10^{14}	0.80	29.932±0.004°	0.715±0.009°	62.242±0.009°	1.373±0.020°
1×10^{15}	0.73	29.935±0.008°	0.743±0.017°	62.253±0.015°	1.506±0.032°
2×10^{15}	0.81	29.932±0.007°	0.731±0.007°	62.240±0.009°	1.353±0.021°

Fig. 1 shows the saturation moment (M_S) of a ~30 nm MnAl film as a function of total fluence. The saturation moment M_S of MnAl prior to irradiation was ~ 300 emu/cm^3. The value of M_S did not change monotonically and reached a minimum at the fluence of 1×10^{14} cm^{-2}. The H^+ irradiation induced the increase in M_S that reached ~380 emu/cm^3 at the total fluence of 2×10^{15} cm^2. This represents a ~ 27 % increase in the total magnetic moment as the result of ion irradiation.

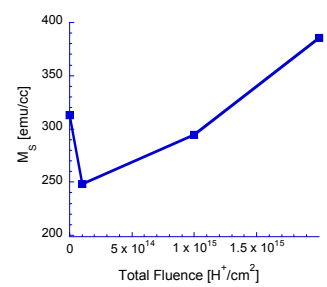

Figure 1. Saturation moment as a function of total fluence

To further investigate the details of magneto-transport properties of proton irradiated MnAl films, the anomalous Hall effect (AHE) was measured from the Hall devices. The anomalous Hall resistance was determined by the spin dependent scattering of charge carriers, i.e. electrons for MnAl by the spins carried by Mn ions. Fig. 2 indicated the strong correlation between the magnetization and the anomalous resistance. A small increase in the AHE resistance for the total fluence of 1×10^{15} cm^3 was observed but is likely caused by the error introduced during the wire bonding process that was required to measure the resistance in the magnetic field. Besides the robustness in magneto-transport property, the film also exhibits a high tolerant to such irradiations, as there are small changes in electrical resistivity. In general, energetic particle irradiation of any ordered film leads to increased disorder, which in turn causes a broadening of the X-ray diffraction peaks. In the present case, the FWHM of the (001) MnAl peaks were about 0.7° prior to irradiation. This is larger than

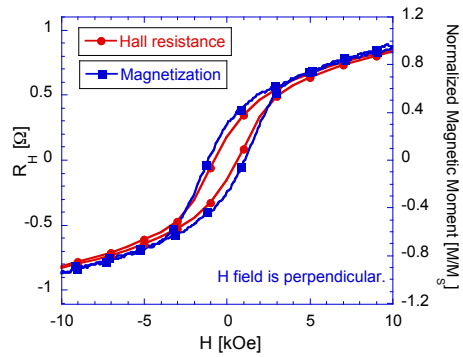

Figure 2. Hall resistance and the magnetic moment (measured by Magneto-Optical Kerr effect) as a function of the external magnetic field. The magnetic field is perpendicular to the film surface and the electric current.

the ~0.287° expected for a perfect film, due in part to larger-scale flaws such as mosaicity, and crystallite size. Further broadening, as listed in Table 1, is caused by the introduction of crystal defects, such as dislocations and grain boundaries, which can be associated with the displacement damage caused by proton-induced cascade events. It is also worth noting that the peak broadening reached a maximum at $\Phi = 1 \times 10^{15}$ H^+/cm^2. The enhancement in the coercivity can also be attributed to the addition of crystal defects, which often acts as the pinning sites for the domain walls.

With the increase in the fluence to 2×10^{15} H^+/cm^2, the effect of displacement damage was overwhelmed by the ordering enhancement in $L1_0$ MnAl, which was observed both in the change of $\boldsymbol{S}$, M_{Sat} and the FWHM of MnAl peaks. Since no *in-situ* heating was provided to assist diffusion, the chemical ordering in the MnAl film was not fully recovered to that of the virgin sample. On the other hand, the saturation moment became larger than that of the virgin sample, which implies that there were additional contributions of magnetic moments from the change in the microstructure in $L1_0$ MnAl. This may imply that the defects introduced during the irradiation are ferromagnetic. Another plausible explanation could be strain relaxation caused by added defects and grain boundaries, and M_S in MnAl was strongly dependent on the film strain. The irradiation process caused the change in the peak broadening as aforementioned, and resulted in the relaxation of in-plane strain due to the large lattice mismatch between MnAl and MgO (~6.7%). Thus, the magnetic moment was enhanced despite only a partial recovery of the chemical ordering.

Even though the changes in the microstructure and the resistivity were appreciable during the irradiation process, the AHE at room temperature were very robust, and not significantly affected by the total fluence of proton beam. From the AHE loop, the coercivity (H_C) can be extracted. The lack of change in the coercivity indicates that the perpendicular magnetic anisotropy was not modified by the proton beam, despite the addition of the defects. This is a highly desirable property for applications in harsh radiation environments. It appears, then, that the magneto-transport properties of $L1_0$ MnAl are very resilient to the displacement damage effects caused by 2 MeV proton irradiation.

(ii) Synthesis and irradiation of novel magnetic materials with strong PMA

Amorphous rare earth (RE) transition metal (TM) alloys are known ferrimagnets thanks to the antiferromagnetic coupling of the rare earth element Gd, Tb and the transition metal elements Fe, Co. These RE-TM alloys are promising spintronics materials, especially because of their

ultrafast magneto-optical response. However, the origin of perpendicular anisotropy in these materials is still being debated. Studies have correlated the magnetic anisotropy of RE-TM magnetic films with various structural characteristics. Another attractive feature of RE-TM films is that the magnetization can be tuned, and very low M_s can be obtained, which is desirable for low power spintronic devices. In the theory of amorphous ferrimagnets, the coupling between RE and TM ions is antiferromagnetic. Radiation study not only allows us to investigate the effect of proton beam on the microstructure and the properties of amorphous alloys, but also can be a tool to probe the origin of PMA by modifying short and medium range ordering in these alloys. We have investigated both TbCoFe and GdCoFe systems, and developed a Monte Carlo model to understand the magnetic behaviors in these met-glasses, i.e. amorphous alloys.

Strain-induced enhancement of coercivity in amorphous TbFeCo films:

We have synthesized amorphous TbFeCo with ~ 30 at. % Tb films via the combinatorial growth, and reported the magneto-transport behavior of TbFeCo with perpendicular anisotropy using anomalous Hall effect, and observed a significant increase in coercive field as a function of the width of TbFeCo Hall bars. The enhancement in coercivity was likely linked to the relaxation of compressive strain due to the reduction in the surface stress. The effect of strain and dimensionality on the coercivity in TbFeCo will make it an attractive candidate for future nanomagnetics and spintronics not only for the higher thermal stability (sufficient magnetic anisotropy) in nanoscale devices, but also for the tunable coercivity and the magnetization reversal via the strain or stress (the magnetostriction effect).

Fig.3 shows TEM images of a ~35 nm thick TbFeCo films. No evidence for crystalline structures was observed in the cross-section TEM bright field contrast image as shown in Fig. 3a. High-resolution TEM image (Fig. 3b) showed no nano-crystallites inside the film. Only a single ring pattern was presented in the fast Fourier transform (FFT) image that attributed to the lack of long range ordering. In addition, XRD scans showed that there were no diffraction peaks other than these from the substrate for TbFeCo films with different thickness (not shown here). Both TEM and XRD confirmed the amorphous nature of the film deposited at the ambient temperature, which was consistent with the previous reports on RE-TM films.

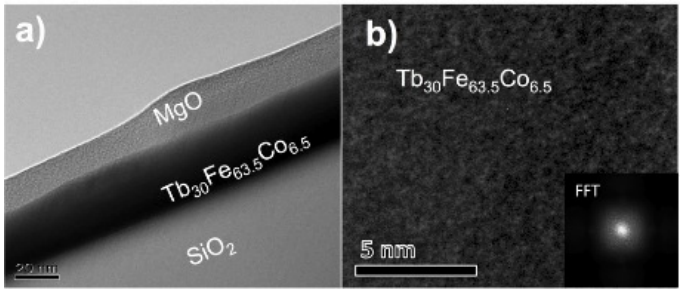

Figure 3. (a) Bright field TEM image of a 35 nm TbFeCo film deposited on SiO_2/Si. A 15 nm MgO layer was used to cap the film; (b) HRTEM image of the TbFeCo film. The inset is a FFT pattern of the image.

Fig. 4a shows hysteresis loops of a 35 nm thick TbFeCo film. The saturation moment (M_s) was ~ 100 emu/cc. The small saturation moment was due to the ferrimagnetism of amorphous

RE-TM alloys. Co and Fe ions have a small single ion anisotropy and Tb ions have large anisotropy. The large TM-TM ferromagnetic interaction aligns the magnetic moments among Fe and Co ions, while the large anisotropy of RE ions fans the magnetic moments of Tb out over the opposite hemisphere. As a result, the net moment was the difference of magnetic moment between Tb and Co/Fe. The out-of-plane coercive field (H_C) of this sample was ~ 0.66 T and magnetic anisotropy field (H_K) was ~ 1.6 T. From the hysteresis loops one can estimate the anisotropy energy (K_U) ~ 0.8 x 10^6 erg/cc that was out of the plane.

Fig. 4b shows the Hall Resistance (R_H) as a function of an external magnetic field, which was applied perpendicular to the film plane, for 50 and 500 μm wide Hall bars at room temperature. There was a significant difference in H_C for two different Hall bars measured via this method. The magnetic field dependence of Hall resistances for both Hall bars resembled the hysteresis loop of out-of-plane magnetization of the samples, which was due to the dominance of the anomalous Hall resistance (R_{AHE}) over the ordinary Hall resistance (R_{OHE}). R_{AHE} was proportional to the magnetization (M) of the ferromagnet, thus it was strongly dependent to the magnetic field. Based on the relationship between R_{AHE} and M, the values of H_C of Hall bars were extracted as a function of the width of Hall bar. For the 500 μm wide Hall bar, H_C was 0.6 T that was close to the value (~0.66 T) measured from out-of-plane hysteresis loop that was consistent with the value measured on unpatterned film by VSM and MOKE. In contrast, H_C was increased to ~2.1 T when the width of the Hall bar was reduced to 50 μm, representing a three fold increase over H_C measured from both 500 μm wide Hall bar and the unpatterned film.

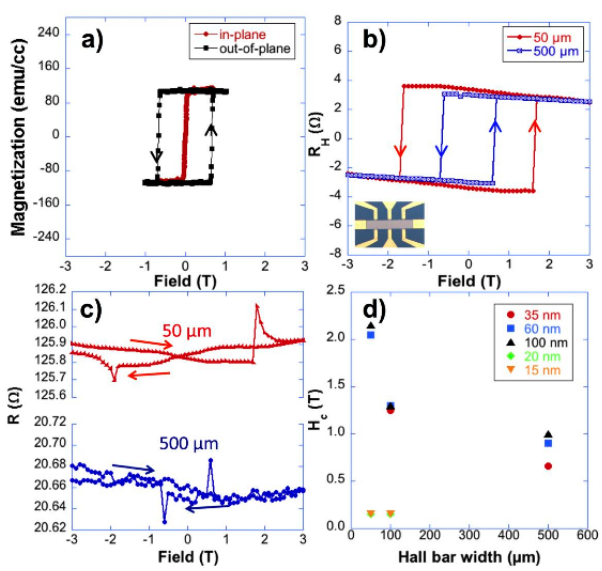

Figure 4. (a) Hysteresis loops of a 35 nm TbFeCo film measured at room temperature; (b) Hall resistance vs. magnetic field for two Hall bar devices with the widths of 50 and 500 μm. The inset is an optical image of a Hall bar device; (c) Magneto resistance vs. magnetic field for two Hall bar devices with the widths of 50 and 500 μm; (d) Coercive field vs. the width of Hall bar for TbFeCo films with various thicknesses measured at room temperature

Similar size dependence was also observed in the magneto-resistances of these two Hall bars, as shown in Fig 4c. Two sharp peaks were observed at the magnetic fields corresponding to H_C in AHE loops shown in Fig 4b. As the magnetic field increase in the positive direction, the resistance remained almost constant up to the positive H_C where resistance suddenly increase creating a positive sharp peak, then the resistance decreased to almost the same value as before and remained constant value through the maximum 3 T. The same MR behavior was also observed as the magnetic field decrease. There was also a sharp peak at negative H_C. However,

this peak was negative.

These two antisymmetric magneto-resistance peaks were also observed in Pt/Co multilayer structures with PMA. MR peaks are strongly related with the domain number per unit area, and occur near the coercive field as a result of multi-domain state of the film during the magnetization reversal process. The opposite magnetizations across the domain wall cause the opposite Hall fields. This induced the circulating current around domain wall, leading to the redistribution of MR peak and electric field. The antisymmetric MR indicates that domain wall direction is in the film plane and is perpendicular to the current direction. Nonetheless, the occurrence of MR peaks at H_C confirmed the strong size dependence of coercivity in amorphous TbFeCo. On the other hand, the MR ratios for 500 μm and 50 μm were similar, 1.4 % and 1.6 % respectively, which was likely due to the similar densities of magnetic domains as previous reported.

Additional study on the effect of the film thickness was also performed. Fig 4d shows H_C as a function of Hall bar width measured at room temperature while the thickness of TbFeCo was changed from 15 nm to 100 nm. The unpattern films coercivity increased from ~0.2 T for a 15 nm thick TbFeCo film to 1 T for a 100 nm TbFeCo film monotonically. The coercivity reached a plateau showing a very small change as the thickness of the film increased from 60 nm to 100 nm. The effect of film thickness on the enhancement of H_C in the TbFeCo Hall bar was studied. We observed the similar enhancement in coercive field as width of the Hall Bar is reduced except for the 15 nm and 20 nm thick films, in which H_C remained the same as unpatterned films.

In the absence of magneto-crystalline anisotropy, the enhancement of coercivity may be explained by the stress-induced anisotropy in amorphous TbFeCo films due to the relaxation of compressive strain in Hall bar devices thanks to the large magnetostriction effect. The magnetostriction effect on the perpendicular magnetic anisotropy has been shown for various magnetic thin films. In particular, Saito et al. have shown that the tensile strain in DyFeCo alloy modulated the easy axis of magnetization[10]. Amorphous TbFeCo films experienced compression resulted from incorporation of excess atomic density due to the surface stress. In contrast, the tensile strain in amorphous film typically resulted in nano-voids, which was not observed in TEM images. The compressive strain in the film was bi-axial and was partially relaxed in the Hall bar structures due to the reduction in the surface stress. The relaxation of compressive strain resulted in the increase in the coercivity of TbFeCo films. The surface stress was reduced further with the width of Hall bar, giving rise to the width dependence of the coercivity in the films thicker than 30 nm. In comparison, we did not observe any effect of the strain relaxation in the 10 and 20 nm films probably because the width of Hall bars was not small enough to release the surface stress significantly.

Displacement damage in RE-TM thin films: Amorphous TbCoFe films were irradiated the same fashion as MnAl. The characterization of the magnetic and magneto-transport properties

has been undergoing. The properties were significantly affected by the proton, particularly the magneto-transport property.

Fig. 5a shows hysteresis loops TbFeCo film with thickness 35 nm at room temperature. The saturation moment (M_S) was ~ 100 emu/cm^3. The small saturation moment was due to the ferrimagnetism of amorphous RE-TM alloys where the net moment is difference of magnetic moment between Tb and Co/Fe. The out-of-plane coercive field (H_C) of this sample was ~ 0.66 T. In-plane VSM shows that the saturation moment increase monotonically with the total irradiation fluence. The saturated moment is increase from 100 emu/cm^3 up to 180 emu/cm^3 as shown in Fig. 5b).

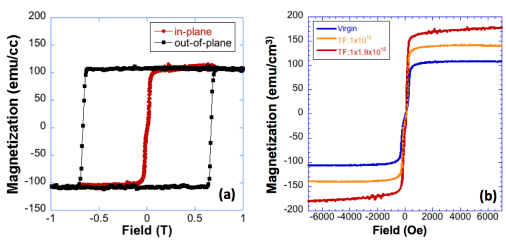

Figure 5. a) Hysteresis loops of virgin sample shows strong perpendicular magnetic anisotropy with the saturation moment M_S ~ 100 emu/cm^3 and out-of-plane coercive field H_C ~ 0.6 Tesla b) The saturated moment increases monotonically after irradiation.

Transport measurements including Hall measurement and resistivity were measured as a function of temperature. The resistivity of sample increased monotonically with the total fluence, suggesting that the irradiation cause the films to become more resistive. The Hall resistances as a function of magnetic field resembled the hysteresis loop of out-of-plane magnetization of the samples, implying the domination of anomalous Hall effect (AHE) over ordinary Hall effect (OHE). The values of coercive field of Hall bars were extracted as a function of the width of Hall bar. Due to the large magnetostriction of TbFeCo and the film was partially relaxed from surface stress reduction during Hallbar fabrication, only 500 μm wide Hall bar represents coercivity of the as-deposit film (not shown here). Hall resistance was measure as a function of applied magnetic field perpendicular to the film plane at temperature ranging from 50K to 300K. Fig. 6a shows coercivity *(H_C)* of a 500 nm wide Hall device before and after irradiation as a function of temperature. The irradiation effect on coercive fields shows similar trend—increasing H_C. The coercivity enhancement due to irradiation in magnetic materials usually associated with the magnetic domain wall pinning during magnetization reversal in which irradiation-induced point defects act as pinning sites. In amorphous materials, which already have highly degree of disorders, having domain pinning defects alone to describe the coercivity changes is unsatisfying. Besides coercive field enhancement, we also observed the reverse polarity of the Hall loop around 250K in 500 nm wide Hall bars after irradiation (not shown here). Later we determined that the temperature where the Hall loop sense change polarity is compensation temperature T_{comp}. The coerevity increased rapidly and diverge at T_{comp}.

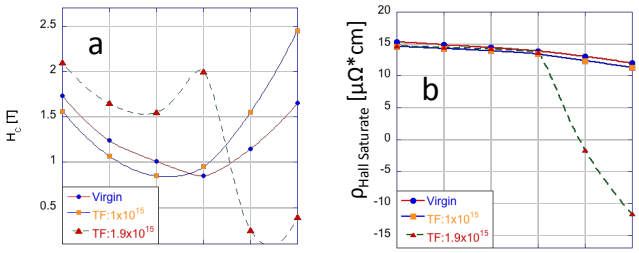

Figure 6. a) Coercive field and b) Hall resistivity as a function of temperature from a TbCoFe Hall device as a function of fluence. The device width is 500 nm.

Temperature dependent of spontaneous anamolous Hall resistivity $\rho_H(T)$, which reflects temperature dependent of the sublattice magnetization, was further investigated. The contribution of each sublattice to hall resistivity has not been fully clarified. According to Malmhall's report, it appears that Fe subblattice has majority contribution to Hall resistivity in amorphous TbFe system. The hall resistivity is determined by $\rho_H = R_H t$ where R_H is the Hall resistance at high field and t is the thickness of the film. Fig. 6b shows the dependent of Hall resistivity (ρ_H) from 50K to 300K of a 500 nm wide Hall device as a function of fluence. The Hall resistivity decreases toward compensation temperature and changes from positive to negative sign after it passed $T_{comp.}$

Despite the same composition and the homogeneity of the film (from TEM result) throughout the experiment, the proton irradiation, known for creating displacement damages, might also alter the short-range-order (SRO) effects which is very important for magnetic properties of RE-TM amorphous materials. We employed the Stopping and Range of Ions in Matters (SRIM) simulation to study microstructural change during proton irradiation. The simulation results are shown in Fig. 7. It shows both small cascades (typically for 2 MeV proton) along the path of the proton beam, as well as large cascade events that only occur in TbFeCo layer after total events of $4x10^5$. The estimated volume of cascades is 3645 nm^3. It also indicates that the large cascades dominate Tb, Fe, and Co recoiled distribution. Such large cascades can leave behind large voids or clusters that can effect the local composition of TbFeCo after irradiation. As a result of microstructural change, SRO is likely altered. Hence, the magnetic properties are modified as a result of SRO or pair ordering modification. The change of surface to volume ratio is related to "effective" composition in which control the SRO.

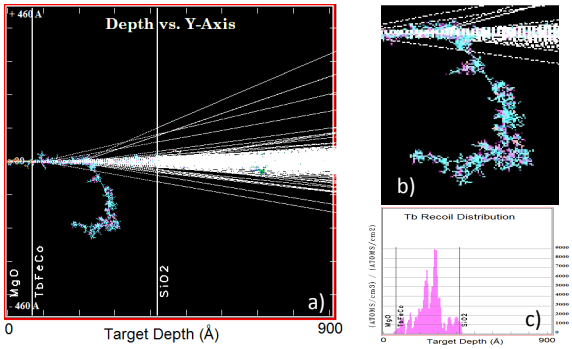

Figure 7. SRIM simulation results: a) depth profile of film structure reveals large cascades in TbFeCo layer b) Zoom-in image of the large cascade c) Tb recoil distribution is influenced by the large cascade signature.

Monte Carlo Simulation of PMA origin in RE-TM alloys: Based on our recent published experimental results, the amorphous $Gd_xFe_{93-x}Co_7$ alloy films exhibit perpendicular magnetic anisotropy (PMA) in two different compositional regions (x = 20-34 and 52-59). To understand the compositional and temperature dependence of the magnetization, series of Monte Carlo (MC) simulations have been made.

The Monte Carlo simulations are based on an atomistic model. In lieu of an amorphous structure model for GdFeCo, we believe that the essential physics can be captured by considering a model of random crystalline alloy. In the latter model, classical Heisenberg spins, representing Gd, Fe and Co, are randomly located at the sites of a face centered cubic lattice. The atomic concentrations are fixed by the alloy composition. The Hamiltonian including the local anisotropy is employed to calculate the energy for each possible spin configuration:

$$H = -\frac{1}{2}\sum_{<i,j>} J_{ij}\vec{S}_i \cdot \vec{S}_j - \sum_{i=1}^{N} D_i\left(\vec{S}_i \cdot \vec{n}_i\right)^2 - \sum_{i=1}^{N} \mu_i \vec{B} \cdot \vec{S}_i.$$

The subscript i is index of the lattice site. The spin $\vec{S}$ is normalized to a unit vector. The first term is summed over all the nearest neighbors of each lattice site. The exchange constants J_{ij} and moment μ_i are summarized in the table below. To obtain a consistent (low) magnetization with the experimental data, we find it necessary to assume Gd spins having a non-collinear sperimagnetic structure, which origins from the anisotropy term. The local uniaxial anisotropy strength is denoted by D_i. $\vec{n}_i$ is the unit vector characterizing the random easy axis of the ith spin.

$\boldsymbol{J_{Gd-Gd}}$	$\mathbf{1.26\times 10^{-21}}$J	$\boldsymbol{J_{Gd-Fe}}$	$\mathbf{-2.73\times 10^{-21}}$J	$\boldsymbol{\mu_{Gd}}$	$\mathbf{7.63\mu_B}$	$\boldsymbol{D_{Gd}}$	$\mathbf{1.68\times 10^{-20}}$J
J_{Fe-Fe}	4.5×10^{-21}J	J_{Gd-Co}	-6.75×10^{-21}J	μ_{Fe}	$2.217\mu_B$	D_{Fe}	0
J_{Co-Co}	4.62×10^{-21}J	J_{Fe-Co}	5.51×10^{-21}J	μ_{Co}	$1.71\mu_B$	D_{Co}	0

The thermodynamic equilibrium at each temperature, corresponding to the minimization of the free energy of the system, was obtained by the standard Metropolis algorithm. In the simulations, the lattice size was set to $50\times50\times50$ together with a periodic boundary. At each temperature, 10^8 MC steps were performed to reach the equilibrium and the magnetization was averaged over the next 10^8 MC steps.

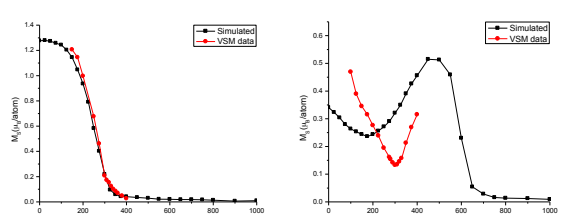

Figure 8. Simulated curve and VSM data for $Gd_{57}Fe_{36}Co_7$ (Left) and $Gd_{21}Fe_{71}Co_7$ (right)

For $Gd_{57}Fe_{36}Co_7$, the simulated curve is in good agreement with experimental data from the VSM measurement, as shown in Fig. 8. As for $Gd_{21}Fe_{71}Co_7$, the VSM data shows a compensation temperature at 310K. Due to the concentration variation, we can adjust the exchange constants. After multiple simulations, $J_{Fe-Fe} = 3.0\times10^{-21}$J and $J_{Gd-Gd} = 2.52\times 10^{-21}$J are selected. By setting the Gd anisotropy strength to $D_{Gd} = 5.04\times10^{-20}$J, we obtained the corresponding simulated curve. Even though the curve shows a compensation feature, there remains a discrepancy between the simulation and measurement as shown Fig. 5.

In summary, the result of the Monte Carlo simulation matches the experimental data for $Gd_{57}Fe_{36}Co_7$; however, for $Gd_{21}Fe_{71}Co_7$, The model and parameters need to be refined to obtain consistent results.

(iii) Synthesis and Characterization of PMTJ devices

For this reporting period, major activities at Grandis were focused on perpendicular magnetic tunnel junction (PMTJ) stack development and optimization; and device integration process improvement; as well as extensive film level and device level characterization. The following discusses in detail about these activities and results. The half structure, and full structure PMTJ films were irradiated and systematically characterized by Lu group at UVA and B. Weaver at NRL.

PMTJ stack development: The specific objectives of PMTJ stack development are to provide a baseline PMTJ stack for device processing, so that spin transfer torque (STT) switching properties can be evaluated. The PMTJ free layer needs to have thermal stability factor (delta) value greater than 40 in order for information to be retained for 10 years. At film level, this means that the free layer needs perpendicular anisotropy field (H_k) greater than 1 kOe. The PMTJ reference or pinned layer needs to have a much larger H_k and H_c field values than those of the free layer. When one single perpendicular pinned layer is used, it exerts a large perpendicular biasing field to the free layer, causing the latter to have non-symmetric switching fields or only one memory state. To avoid this problem, a synthetic antiferromagnetically (SAF) coupled pinned layer needs to be developed. The MgO tunnel barrier needs to be optimized so that the resistance and area product of the PMTJ film is less than 20 ohm times micron squared in order for the STT switching voltage to be much less than the MgO tunnel barrier breakdown voltage; and the TMR ratio needs to be greater than 100% to have fast memory read speed and high spin transfer efficiency, so that the STT switching current density and voltage can be low enough for reliable and repeatable device writing operations. Over the past year, we have worked on improving the free layer, the SAF reference layer, and the MgO tunnel barrier. Representative results are discussed below.

We deposited a film stack of Ta 30/CoFeB 10.5/MgO10/CoFeB 12/Ta-4 Wedge/Co 5/ Pt 10/[Co 2.5/Pd 10]7/Co 5/Ru 8.3/Co 5/[Pd 10/Co 2.5]10/Pd 10/Ta 50/Ru 100 (Å). The CoFeB 10.5 Å below the MgO 10 Å tunnel barrier is the free layer. The CoFeB 12 Å above MgO has weaker perpendicular anisotropy, so it is exchange coupled through a thin Ta wedge layer. The wedge layer has varying thicknesses across the 300 mm wafer, so that we can investigate Ta

thickness effects on the wafer by testing different locations. Above the Ta wedge layer, we built a SAF coupled perpendicular reference or pinned layer.

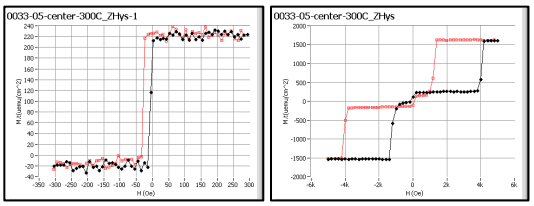

Figure 9. Minor (left) and major (right) M-H loop of center location for Ta-wedge wafer.

After annealing at 275°C for two hours, the M-H loops of the center Ta 4A location are shown in Fig. 9. The major loop is shown on the right hand side, while the minor loop for the free layer only is shown on the left side. At film level, the free layer H_c is less than 20 Oe; while the reference layer switches at 1.5 kOe to 4 kOe. The low H_c for the free layer is caused by domain formations. After patterning, the free layer is expected to have H_c greater than 1 kOe, because the measured film H_k value is near 5 kOe. Since the film level free layer switching field is well separated from those of the reference (or pinned) layer, film level CIPT (current in-plane tunneling) testing can be performed to measure PMTJ film TMR and RA performances without going through device patterning. The results are shown in Fig. 10.

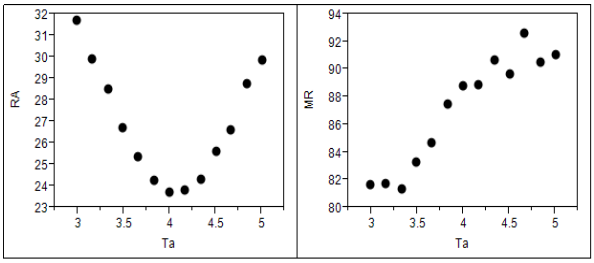

Figure 10. RA (Wmm^2) and MR (%) data after 275°C 2 hours annealing for Ta wedge wafer.

The left plot in Fig. 10 shows the RA (Wmm^2) value dependence on Ta thickness (A). Ta of 4A is at the center of the 300 mm wafer. The RA value is mainly controlled by the MgO tunnel barrier thickness. At wafer center, our rf-MgO film thickness is thinner than wafer edge, therefore we observed a minimum RA value. The magnetoresistance (MR) or tunneling magnetoresistance (TMR) data are shown in the right plot of Fig. 10. TMR ratio greater than 90% is observed for Ta thicker than 4A. It was known that Pd in the top SAF pinned layer can diffuse into the MgO barrier upon annealing, thus severely degrades the TMR ratio. The Ta in between the top CoFeB layer and the Co/Pd SAF layer is critical in blocking the diffusion of Pd to MgO, and maintain high TMR ratio after annealing. Annealing is necessary to transform the MgO and amorphous CoFeB into matching (001) crystal orientation for high TMR ratio and spin torque efficiency. But this Ta layer cannot be too thick, since it also acts like an exchange layer to allow magnetic exchange coupling between the top CoFeB layer and the Co/Pd perpendicular

SAF layer. The top CoFeB layer is weakly perpendicular, it is made into a strongly perpendicular reference or pinned layer by coupling to the Co/Pd SAF layer.

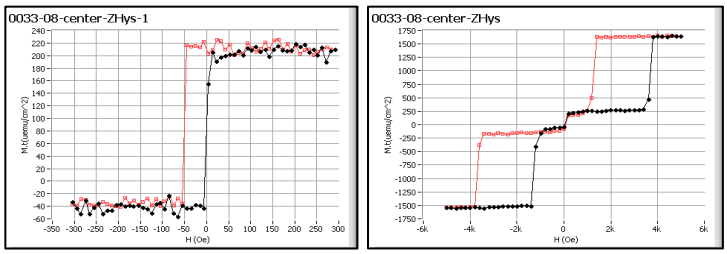

Figure 11. Minor (left) and major (right) M-H loop of center location for CoFeB wedge wafer.

To further increase the thermal stability of the free layer, we explored inserting thin Ta layer within the CoFeB free layer. We deposited a film stack of Ta30/CoFeB 8W/Ta 3/CoFeB 8W/ MgO 11/CoFeB 12/Ta 4/Co 5/ Pt 10/[Co 2.5/Pd 10]7/Co 5/Ru 8.3/Co 5/[Pd 10/Co 2.5]10/Pd 10/ Ta 50/Ru 100(A). A wedge thickness layer was applied to the CoFeB free layer below and above the Ta 3A insertion layer across the 300 mm wafer. The center location M-H loop data are shown in Fig. 11. Similar to the M-H loops shown in Fig. 9, the free layer and reference (pinned) layer switching fields are well separated. Although as previously commented, free layer film level switching field (Hc) is much lower than its device switching field due to domain formation; free layer having Ta insertion layer has nearly doubled Hc value at film level.

The RA and MR test data of this wafer are shown in Fig. 12. The wafer center CoFeB thickness is 8 Å. Like Fig. 10 left plot, RA showed a minimum value at wafer center due to MgO tunnel barrier thickness thinner at wafer center. The maximum MR or TMR ratio above 90% at CoFeB thickness between 8 to 9 Å is observed. As the CoFeB thickness increases from 6 to 9 Å, the MR increases as expected; since film property such as magnetic polarization and magnetization degrades when the film thickness is below 20A. The sudden drop of MR ratio above CoFeB 9 Å is due to the loss of interfacial perpendicular anisotropy (PMA) of the CoFeB free layer.

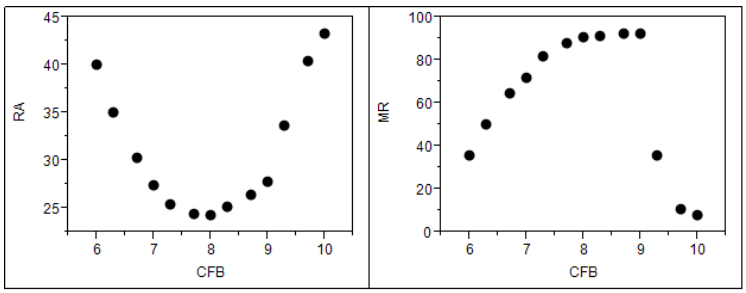

Figure 12. RA (Wmm^2) and MR (%) data after 275°C 2 hours annealing for CoFeB wedge wafer.

In summary, the PMTJ stack developed is adequate for evaluating STT switching performances. The film TMR ratio for above films is about 100%. PMTJ film sample 10266-02

was subjected to 2 MeV proton irradiations with a dosage of 1E15 /cm^2 at NRL. CIPT re-test at Grandis found the sample having a TMR ratio of 100.1% and RA=8.9 ohm/um^2; and Sample 10270-02, with a radiation dosage of 1E14 /cm^2, having a TMR=92.6%, and RA=7.0 ohm/um^2. TMR and RA values of these two samples seemed to have survived the radiation treatments.

Device integration process improvement: Targets for this project are to use a standard wafer fabrication process to produce a repeatable and robust device fabrication method with varying MTJ sizes. Final yield and device size are determined by the processing steps and margins involved. Final yield on wafers were better than 90% at a smallest node of 65nm cells, which was achieved with the implementation of new process integration. Under this project, in the past year, we have improved our device process flow as illustrated in Fig. 13, significantly reduced device-shorting problems, and produced PMTJ device wafer for radiation studies.

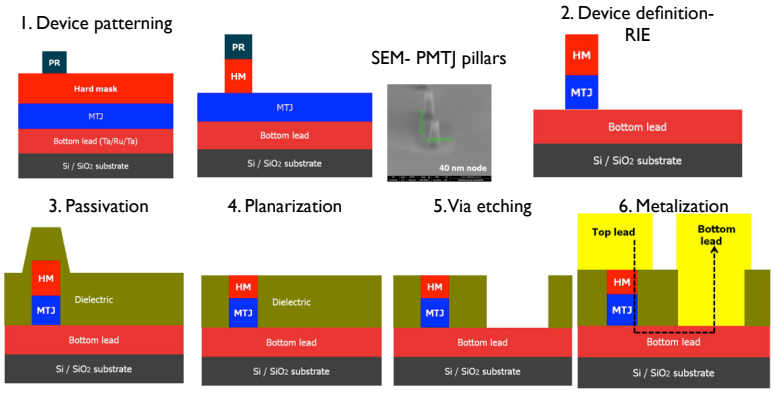

Figure 13. Flow chart of PMTJ fabrication process.

Device patterning: Four inch wafers are utilized for fabrication due to the tooling used in this process which is based on a 4" wafer size. Wafers arrive with MTJ device film deposited over entire wafer. A high deposition rate physical vapor deposition (PVD) was utilized to deposit a thick hard mask (HM) material. Any material may be utilized for HM which has a low ion mill etch rate such as tantalum. Wafers are first patterned with Ebeam at varying sizes (40nm-500nm) using an electron beam sensitive photoresist (PR) spin coated over the wafer. This will act as a mask for the HM etching which is done in a reactive ion etch (RIE) system. The HM has a dual purpose; one it will be used to protect the device against ion milling which will define the final device size and two, this will act as the connection point for the top lead of the final device. After RIE the printed design and HM size are matching meaning a 40nm node is 40nm after RIE.

Device definition: Once HM has been defined, device is ready for ion milling. Angle, power, and end point must be optimized to reduce shunting caused from re-deposition. Re-deposition cannot be eliminated as ion milling by design is a physical removal process. As the device is milled, etched material is coated on the sidewall of the device. This causes the dimension of device to grow from 40nm to about 65nm. After ion mill, device must be isolated from the environment and provide a separation between top and bottom lead in final device fabrication by a plasma-enhanced chemical vapor deposition (PECVD). The material must be dielectric to eliminate electrical contact from top and bottom lead. With the device now isolated, the wafer

must be planarized to open the top lead of the device. This is done by chemical mechanical polishing (CMP) which polishes the higher points at a faster rate and allows for a flat surface.

Device connection: With the device planarized, electrical connections need to be made to for final testing. Photoresist is spun over the entire wafer. A photo mask is used to expose a bottom electrode in the photoresist with a specific pattern. After hardening of the resist the dielectric is etched to expose the bottom electrode by RIE. With the bottom lead exposed, a second photoresist is spun over the wafer and exposed to open up the top and bottom lead at the same time. The top and bottom lead are deposited in a PVD system with any material which is conductive. After deposition the metal is lifted off and this now makes an electrically active device that is ready for testing. Fig. 14 shows an optical image of part of device wafer and a bright field TEM image of a finished MTJ stack.

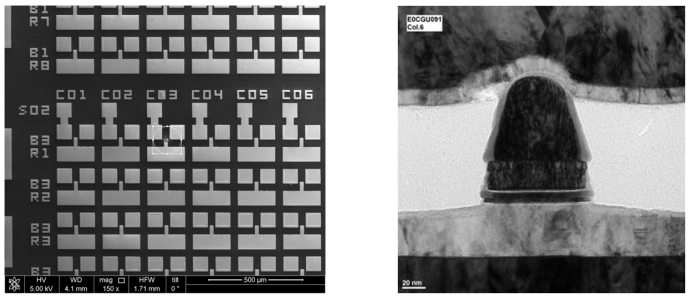

Figure 14. Top view (left) of device wafer and cross-section (right) of a finished PMTJ device.

Characterization of PMTJ devices:

Device level measurements were routinely done to evaluate open and shorting performances of our processed PMTJ device wafers, TMR and RA parameters of PMTJ devices, and STT switching performances of PMTJ devices. Our device wafers consist of 16 dies (or blocks). There are various designed device sizes within each die (block). Either very high or very low resistance values indicate open or shorting problems. Right plot in Fig. 15 shows a good device wafer largely free of open or shorting problems. The measured TMR and R (low) value for circular devices varied as a function of design widths (diameters), and some 40nm (design) devices have TMR ratio greater than 100%.

STT switching was performed, and calculated critical current density J_{c0} values are shown in Fig. 15. Average STT critical switching current density is about 4 MA/cm^2 for 30nm devices. This wafer is ready to be delivered for radiation studies at NRL and University of Virginia.

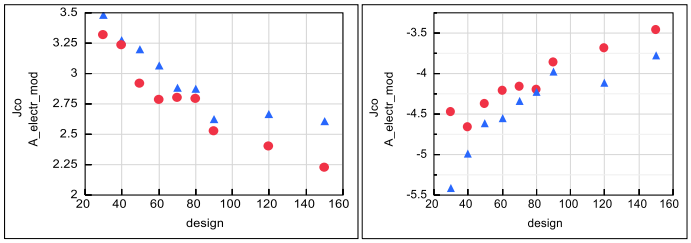

Figure 15. STT switching current density versus device widths.

(iv) Displacement and ionization damages of PMTJ devices

We evaluated the effect of displacement damages on the microstructures and physical properties of the full structure of PMTJ wafers in order to understand the changes in structure and properties related to the individual layers and the interfaces. 2-MeV protons were chosen to investigate the effect of displacement damages on the microstructure and physical properties. An initial fluence Φ of 10^{14} H^+/cm^2 was chosen in order to establish a baseline for the radiation response. Later we increased the doses up to $5x10^{15}$ H^+/cm^2 to establish the failure threshold for the PMTJ. The experiment is still on going as we keep increase the fluence of proton in these samples.

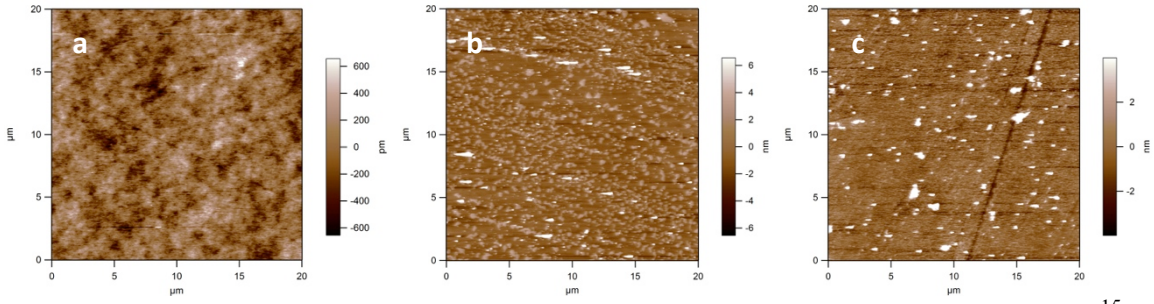

Figure 16. AFM images of a typical PMTJ wafer: a) unirradiated, b) Total Fluence $1x10^{15}$ H^+/cm^2 and c) Total Fluence $5x10^{15}$ H^+/cm^2 respectively.

The samples were irradiated with 2-MeV proton at initial total fluence of $1x10^{14}$ H^+/cm^2. Then the same set of samples were then re-irradiated incrementally until total fluence (TF) is $5x10^{15}$ H^+/cm^2.

PMTJ#1: 1st irradiation TF: $1x10^{15}$ and 2nd irradiation TF: $5x10^{15}$

PMTJ#2: 1st irradiation TF: $1x10^{14}$ and 2nd irradiation TF: $1x10^{15}$

Surface Morphology: As received PMTJ samples are very smooth with RMS roughness of ~ 0.2 nm. After irradiation, similar features as seen in half structure samples are formed at the surface of the films with height 5~60 nm. Consequently, the surface roughness of the films increases to ~ 3 nm.

X-Ray Reflectivity: Figure 19 shows X-ray reflectivity and its corresponding FFT of 2 PMTJ samples. The X-Ray photon intensity decreases after irradiation due to surface roughness. The normalized reflectivity data did not shown significant change due to the irradiation. The corresponding FFT once again show affected of irradiation on capping layer and seeding layer of the PMTJ structure. The dash line is guided to the eyes representing the interfaces of Ta capping layer/CoFeB and Co/Ta seeding layer. Nevertheless, the magnetic layers seem to be unaffected. The defects formation mechanism remains unclear. We speculate that defects tend to diffuse to interfaces where the surface energy is minimum. It is also possible that the capping and seeding layers act as heat sink in which guide the defects by thermal diffusions.

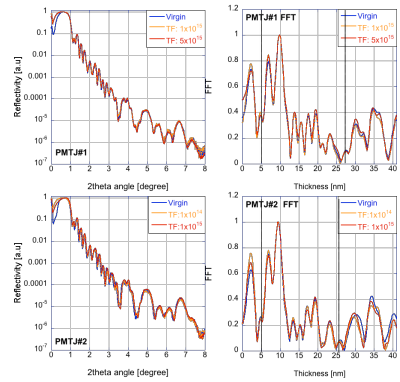

Figure 17. X-ray reflectivity of PMTJ and its corresponding FFT.

X-Ray Diffuse Scattering: Similarly to Half structure XDS results, the intensity of diffused background slightly increase. The normalized XDS plot indicated that there is relatively unchanged in lateral correlation length after irradiation. The results suggest that the intermixing at the interfaces in PMTJ stacks is minimal even with the displacement damages.

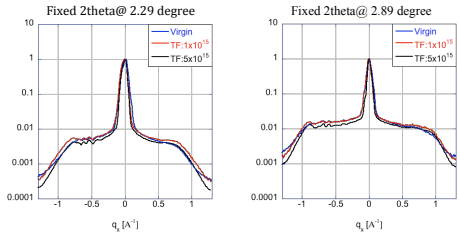

Figure 18. X-Ray diffused scattering curves of PMTJ#1.

Magnetic and transport properties: MOKE was used to measure the room temperature hysteresis loop of PMTJ. The magnetization curve is consistent with the proton fluence up to $5x10^{15}$ H^+/cm^2, indicating the magnetic properties, particularly the perpendicular magnetic anisotropy of PMTJ is very robust to the displacement damages. Tunneling magnetoresistance (TMR) and sheet resistance were measured before and after irradiation. Both PMTJ samples established radiation harden properties. TMR and R_A values were almost the same (within measurement error) throughout each irradiation. TMR ~ 100.1% and R_A is about 8.9 ohm/μm^2 for PMTJ#1 and TMR ~ 98.04% and R_A = 7 ohm/μm^2 for PMTJ#2.

STT switching of PMTJ devcies: A computer controlled pulse generator and source meter are use to characterize retention and functionality of the devices. The operation process is straightforward. A known polarity and magnitude voltage pulse (write voltage) is applied to the device to set the states (high or low current) of the devices. Following the voltage pulse, small DC bias voltage (Read voltage) is applied to read the current therefore determined the state of the devices. The functionality of the devices is performed for 100 cycles by switching the polarity of the write voltage while the read voltage remained the same. The magnitude of the write and read voltage are optimized to ensure switching, minimize noises and eliminate the read-disturb. In

addition, we also performed retention test by measuring 100 repeated reads for each state. (0.7 V-pulse write voltage is used for devices diameter below 500 nm and 1 V-pulse is use for 500 nm devices. The 25 mV read voltage is used for all devices).

The radiation process is done on specific flash field of the wafer. Aluminum mask are used as the radiation shielding material. Devices are shorted to eliminate ESD effect during irradiation. Virgin samples are set at specific states prior to irradiation. After irradiation, each device is firstly go to retention test follow by functionality test.

X-Ray irradiation: 16 Devices are tested. Only 1 device with diameter = 150 nm has failed to retain the pre-set state. Prior to X-Ray irradiation, the device was set at high current state. However, the switching characteristic remains unchanged.

Neon irradiation: Supposedly generate ~ 1500 times more displacement damages than proton's with the fluence = 1 x 10^{11} Neon/cm^2. 3 devices with diameter 60nm, 80nm and 150 nm are tested. Both switching and retention are hold after irradiation.

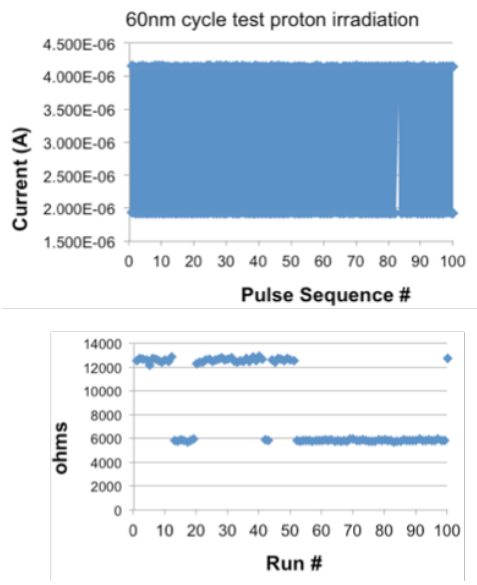

Figure 19. The switching behavior of a 60nm device before (top) and after proton irradiation (bottom). It skips cycle during functionality test, and demonstrates unstable states during 100 read at 25 mV.

Proton irradiation: 7 Devices are tested (60nm, 70 nm, 80 nm, 150 nm, 300 and 2 of 500 nm). Three smallest devices are failed to retain the pre-set state. The 60nm device shows unstable behavior as shown in Fig. 19. The devices randomly switch between high current state and low current state during the 100 repeated reads at only +25mV in which the read disturb is irrelevant for virgin devices. The corresponding functionality test shows that device at some point not switching after applying the write pulse. The 80 nm device has similar behavior. It changes the pre-set state. The switching during retention test is also observed, however, the device only switches once and remains stable throughout the rest of the reads. The 80nm device also skips a cycle during switching test. The 60nm device is also change from the pre-set state. However, both retention and functionality tests are good—no skip cycle and switching states during read.

X-Ray+Neon (higher fluence): Note that all devices in which exposed to X-ray at the first irradiation are pre-set to low current state. Then Neon with higher fluence (1x10^12/cm^2) are use to ensure more hits, thereby, creating mainly displacement. 6 devices are tested. Both functionality and retention remains unchanged.

In summary, heavy ion Neon irradiation intended to create displacement damages. However, the devices are "Rad Hard" as both functionality and retention are unchanged. That leads us to look at the ionization damage. X-Ray, which is low energy photon, are likely to interact with material via photoelectric effect. Photon energy can ionize electron where it could lead to

creating electron-hole pairs—temporary enhance conductivity. We did observe the higher current read on many devices compared to virgin. However, we cannot be conclusive due to the variation of the probe pressure might be the role as well. Similarly protons radiation which energy can be transfer to ionized electron while the remaining energy can be transfer to non-ionized event to displace atoms. However, the magnetic junction are composed of relatively heavy elements so that the light proton mass wouldn't have much effect on displacement damage. The fact that all the failed devices occurred after X-Ray and proton irradiation leads us to believe that the PMTJ devices are prone to ionization rather than displacement damage.

DEPARTMENT OF DEFENSE

DEFENSE THREAT REDUCTION
AGENCY
8725 JOHN J. KINGMAN ROAD
STOP 6201
FORT BELVOIR, VA 22060
ATTN: A. LYALIKOV

DEFENSE TECHNICAL
INFORMATION CENTER
8725 JOHN J. KINGMAN ROAD,
SUITE 0944
FT. BELVOIR, VA 22060-6201
ATTN: DTIC/OCA

DEPARTMENT OF DEFENSE CONTRACTORS

QUANTERION SOLUTIONS, INC.
1680 TEXAS STREET, SE
KIRTLAND AFB, NM 87117-5669
ATTN: DTRIAC